communications materials

A Nature Portfolio journal

Article

https://doi.org/10.1038/s43246-025-00897-x

Low-loss superconducting resonators fabricated from tantalum films grown at room temperature

Check for updates

Guillaume Marcaud[1], David Perello[1], Cliff Chen[1], Esha Umbarkar[1], Conan Weiland[2], Jiansong Gao[1], Sandra Diez[1,4], Victor Ly[1], Neha Mahuli[1], Nathan D'Souza[1], Yuan He[1], Shahriar Aghaeimeibodi[1], Rachel Resnick[1,5], Cherno Jaye[2], Abdul K. Rumaiz[3], Daniel A. Fischer[2], Matthew Hunt[1], Oskar Painter[1] & Ignace Jarrige[1]

The use of α-tantalum in superconducting circuits has enabled a considerable improvement in the coherence time of transmon qubits. The standard approach to grow α-tantalum thin films on silicon involves heating the substrate, which takes several hours per deposition and prevents the integration of this material with wafers containing temperature-sensitive components. We report a detailed experimental study of an alternative growth method of α-tantalum on silicon, which is achieved at room temperature through the use of a niobium seed layer. Despite a substantially higher density of oxygen-rich grain boundaries in the films sputtered at room temperature, resonators made from these films are found to have state-of-the-art quality factors, comparable to resonators fabricated from tantalum grown at high temperature. This finding challenges previous assumptions about correlations between material properties and microwave loss of superconducting thin films, and opens a new avenue for the integration of tantalum into fabrication flows with limited thermal budget.

Superconducting qubit technology is now an established frontrunner towards the realization of a universal quantum computer[1–4]. However, scalability remains a central challenge for superconducting quantum circuits as thousands of physical qubits are required to generate a logical qubit through quantum error correction[5,6]. In order to reduce the scaling overhead, it is crucial to lower the error rates of the individual physical qubits. Research towards this goal has shown that improvements in the quality of the material surfaces and interfaces, which intrinsically host coherence-limiting defects, are linked to longer qubit coherence times.

The most notable breakthrough in this area of research came from the adoption of the high-critical-temperature phase of tantalum, α-Ta ($T_c \sim 4.4$ K)[7], as the base superconducting layer in transmon qubits[8–10]. The lower microwave loss of α-Ta compared with other elemental superconductors traditionally used in the fabrication of transmon qubits, such as Al and Nb, has been ascribed to the thin and stable native oxide layer that is primarily made of Ta_2O_5[11]. There are two sputtering-based methods known to form α-Ta. One involves deposition at temperatures exceeding 350 °C, and the other at room temperature with the use of a seed layer such as Nb[12,13]. Published studies that rely on sputtering to fabricate Ta-based resonators and qubits suggest that only devices made from films deposited at high temperature (HT) benefit from the characteristic performance boost. Indeed, reported internal quality factors for resonators made from Ta films sputtered at room temperature (RT) on sapphire[14] and silicon[15–18] are in the 10^5 range in the single photon regime, which is about one order of magnitude lower than devices made from HT Ta films[19–22]. However, the HT deposition process has its own drawbacks, such as the incompatibility with low-thermal-budget fabrication flows, the low throughput due to the heating and cooling time, and the potential for additional loss channels associated with the metal-substrate interdiffusion or contamination from outgassing in the deposition chamber.

Here, we report on the fabrication and measurement of Ta-based coplanar waveguide (CPW) resonators made from films sputtered at RT and HT on silicon (001) substrate. The resonators share the same design, measurement conditions, and fabrication process besides the sputtering step, which ensures a clean comparison between the microwave loss properties of the films. We show that the loss at the single photon level is comparable for resonators made from both types of films despite clear differences in their microstructural, chemical, and transport properties.

[1]AWS Center for Quantum Computing, Pasadena, CA, USA. [2]Materials Measurement Science Division, Material Measurement Laboratory, National Institute of Standards and Technology, Gaithersburg, MD, USA. [3]National Synchrotron Light Source II, Brookhaven National Laboratory, Upton, NY, USA. [4]Present address: National Institute of Standards and Technology, Gaithersburg, MD, USA. [5]Present address: Google Research, Mountain View, CA, USA.
e-mail: gumarcau@amazon.com; jarrige@amazon.com

The implications of this finding are twofold. First, it shows that the RT Ta sputtering process is viable for the fabrication of state-of-the-art superconducting circuits. Second, the absence of a clear correlation between the film properties and resonator losses highlights the robustness of the performance of tantalum resonators against variations in the deposition conditions.

Results

Resonator design and measurements

In order to assess the influence of the sputtering method on the performance of superconducting circuits patterned into the Ta films, $\lambda/4$ CPW resonators in the 4.5–6.5 GHz frequency range were fabricated from each type of film, RT and HT, and two design splits were chosen with the gap and trace width ($w_g = w_{tr} = w$) set to $w = 3$ μm and $w = 30$ μm. The two geometries provide a different set of participation ratios for the relevant dielectric regions (substrate, air) and interfaces (metal–air, metal–substrate, substrate–air). See Supplementary Figs. S1, S2 for further details on the design of the resonators and simulation of the participation ratios. This allows us to finely compare the microwave loss between the two types of Ta films when the interface participation ratio is increased for $w = 3$ μm, and assess whether other loss mechanisms start to limit the quality factors of the resonators when the interface participation ratio is reduced for $w = 30$ μm.

Figure 1 presents the loss measured at high power ($\delta_{hp} = 1/Q_{hp}$), at low power in the single-photon regime ($\delta_{1ph} = 1/Q_{1ph}$), and the inferred two-level system (TLS) induced loss at one photon ($\delta_{tls}^{1ph} = 1/Q_{tls}^{1ph}$) for the four material-design configurations. The TLS loss is usually described with the standard tunneling model[23–25] that is characterized by a dependence on electric field intensity, $\delta_{tls} \sim (1 + E^2/E_c^2)^{-1/2}$, where E is the electric field and E_c denotes the critical field at which the TLS bath saturates. As the electric field intensity seen by the average TLS can be related to the circulating power within the resonator, this model allows to extract δ_{tls} from the difference between the loss at low power and high power, as $\delta_{tls} = \delta_{lp} - \delta_{hp}$. The accuracy of this method to extract the materials loss induced by TLS (δ_{tls}^0) is contingent upon saturating the TLS response in both power regimes. This condition is not consistently met in our data at the single photon level, especially for $w = 3$ μm as shown in Supplementary Fig. S4. Accordingly, we limit our comparison of the TLS-induced loss between the two materials to the single-photon regime, $\delta_{tls}^{1ph} = \delta_{1ph} - \delta_{hp}$, which is an underestimation of δ_{tls}^0.

Despite identical designs, the resonators fabricated from HT and RT Ta films have different resonance frequencies, which is particularly evident for $w = 3$ μm in Fig. 1c, d. This shift is induced by the kinetic inductance (L_k) of the films that we estimate to be approximately 400 fH/sq for RT Ta and 50 fH/sq for HT Ta based on the deviation of the measured frequencies from the design frequencies. The medians, interquartile ranges (iqr), and standard deviations (std) of δ_{1ph} and δ_{tls}^{1ph} are summarized Table 1, and are calculated from all 15 to 70 measurements per resonator for each material and design. The losses are plotted as a function of the resonance frequencies to highlight the spread caused by the temporal variations and rule out any frequency dependence.

Both materials match state-of-the-art values of the loss reported for similar designs and frequency on silicon[19], with δ_{1ph} and δ_{tls}^{1ph} of approximately 2×10^{-7} and 1×10^{-7} at $w = 30$ μm, and approximately 3.5×10^{-7} and 3×10^{-7} at $w = 3$ μm. Considering the difference in interface participation ratio due to variations in both the sidewall angle and the silicon substrate etching depth between HT and RT Ta resonators, see Fig. 4c, d, we find that the loss of the two materials are comparable and within the standard deviation of our measurements. More details, including participation ratio simulations and cumulative distribution curves, are provided in Supplementary Figs. S2–S5. We now comment on the variation of the TLS-induced loss as a function of w. Simulations reveal that the interface participation ratios increase by a factor five to six when the resonator gap width is reduced from $w = 30$ μm to $w = 3$ μm, whereas measured δ_{tls}^{1ph} only increases two-fold for HT Ta and four-fold for RT Ta. While these increases in measured δ_{tls}^{1ph} might be underestimated due to incomplete loss saturation at the single-photon level, this disparity between predicted and observed values hints that interfaces may not be the only source of TLS-induced loss in our resonators, with substrate TLSs potentially playing a role.

Our finding that both materials have comparable losses is at odds with two reports of higher losses in resonators fabricated from RT Ta compared with HT Ta. In the first report[14], losses were found to be three times larger for RT Ta on a Nb underlayer compared with HT Ta, which was tentatively assigned to the smaller grains of the RT film. However, we also note that our chips were treated in a buffered oxide etchant (BOE) prior to their packaging and measurement, while those in Ref. 14 were not. A post-fabrication BOE treatment is likely to remove resist residues or dry-etch byproducts on top or embedded into the silicon and tantalum surface oxide layers[22]. If this additional BOE cleaning process is indeed required to obtain comparable losses between HT and RT Ta, it may suggest that the surface of RT Ta films is more prone to fabrication-induced surface defects leading to higher losses before BOE treatment. The second report[15] showed that Q_{1ph} for RT Ta films grown on TiN and TaN underlayers is respectively two and seven times

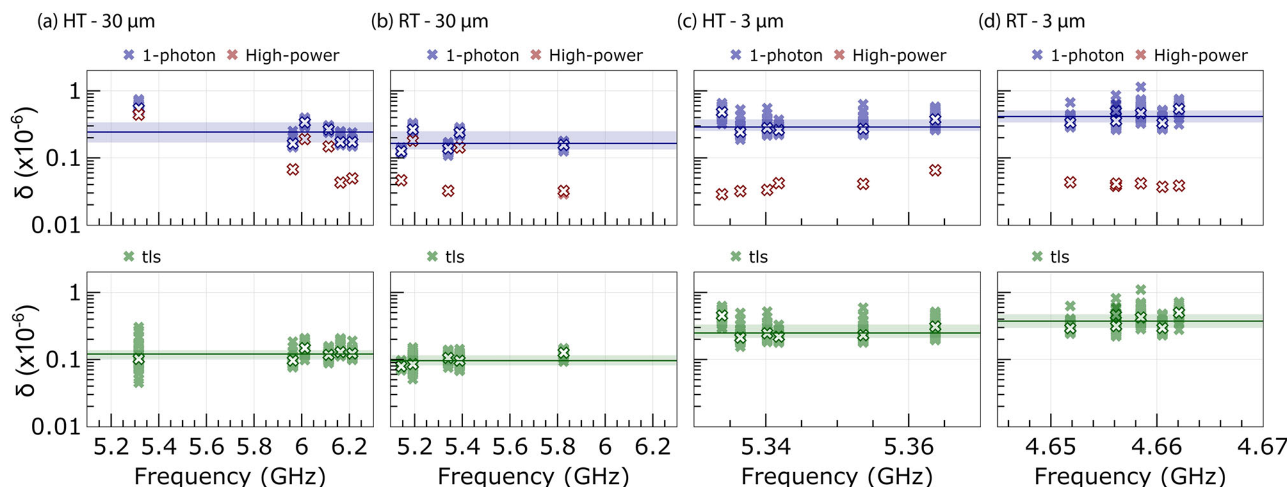

Fig. 1 | Losses of tantalum resonators. Loss measurements at high power (δ_{hp}) and low power in the single-photon regime (δ_{1ph}) (top), and calculated loss induced by two-level systems at one photon ($\delta_{tls}^{1ph} = \delta_{1ph} - \delta_{hp}$) (bottom) as function of resonant frequency for **a** HT Ta - $w = 30$ μm, **b** RT Ta - $w = 30$ μm, **c** HT Ta - $w = 3$ μm, and **d** RT Ta - $w = 3$ μm. The medians δ_{1ph} and δ_{tls}^{1ph} of each resonator are indicated by white markers and the median and interquartile range, also reported Table 1, are represented by a horizontal line and a strip, respectively.

Table 1 | Statistical analysis of resonator losses

	δ_{1ph} (× 10^{-7})			δ_{tls}^{1ph} (× 10^{-7})		
	median	iqr	std	median	iqr	std
HT - 30 µm	2.4	1.7	1.4	1.2	0.4	0.4
RT - 30 µm	1.6	1.2	0.9	1.0	0.4	0.2
HT - 3 µm	2.9	1.3	1.0	2.5	1.2	1.0
RT - 3 µm	4.1	1.7	1.2	3.7	1.7	1.2

Median, interquartile range (iqr), and standard deviation (std) of δ_{1ph} and δ_{tls}^{1ph} for the two materials, HT and RT, and the two geometries, w = 30 µm and w = 3 µm.

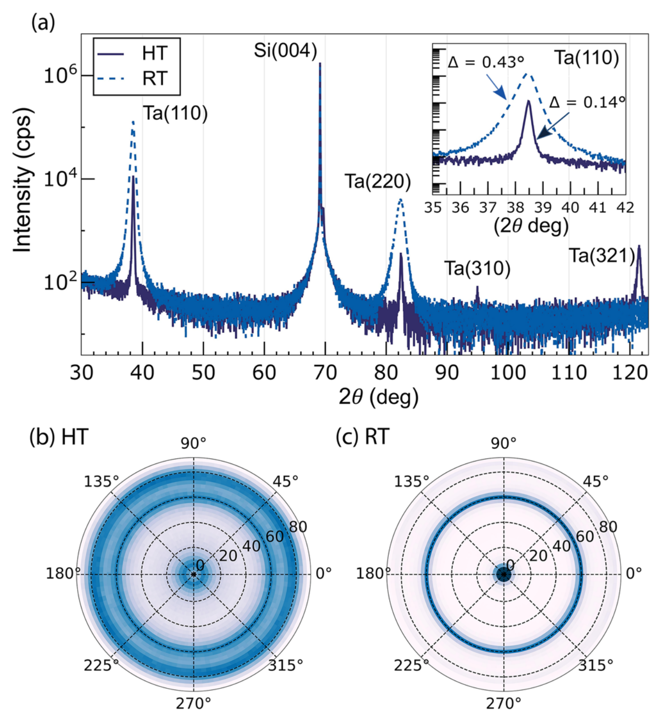

Fig. 2 | Structural characterization. **a** X-ray diffraction 2θ–θ scans showing the growth direction of the tantalum for the two films. A zoomed-in view of the Ta(110) specular reflection is shown in inset. **b**, **c** X-ray diffraction pole figures for HT and RT Ta films, respectively. The color scale represents the intensity of the Ta(110) reflection, with a maximum in dark blue. The ring centered around ω = 75° is assigned to a parasitic in-plane reflection.

smaller than HT Ta, and all devices in this study were treated with BOE prior to packaging. This finding suggests that the material used for the seed layer directly contributes to the loss of the devices, and that TiN and TaN grown on silicon at room temperature can be more lossy than Nb. Nevertheless, since high quality factors in the 10^6 range at single-photon level have been obtained for TiN-based resonators in another study[26], we cannot exclude that a careful optimization of the growth parameters of the nitride seed layers could lead to a reduction of their contribution to the loss.

Materials characterization: structure, morphology, and transport properties

The comparable loss between HT and RT allows us to test long-standing hypotheses regarding the influence of the film microstructure, transport properties, and surface and interface chemistry on the microwave loss[27]. In this section, we focus on the first two. We start with the bulk structural properties of the films measured by XRD. The XRD patterns, shown in Fig. 2a, confirm that there is no trace of spurious β-Ta phase in either film. One of the main differences between the two films is the three-times larger

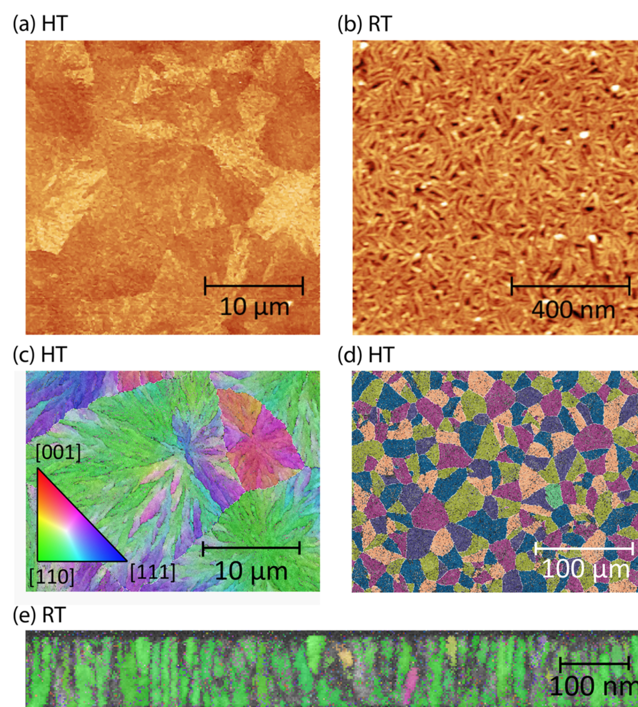

Fig. 3 | Roughness and grain analysis. **a**, **b** AFM topography images of HT and RT Ta films surface, with different field of view and color scale. **c**, **d** Electron backscattering diffraction maps showing (**c**) the color-coded growth direction of few HT Ta grains and **d** the false-color large-scale view of HT Ta grains. **e** Transmission Kikuchi diffraction map of a cross-section of an RT Ta film. The color code represents the growth direction as in (**c**).

full width at half maximum (Δ) of the (hh0) specular reflections along the 2θ axis for RT Ta compared with HT Ta. This can be the result of smaller coherent domain sizes along the growth direction or stronger strain gradient in RT Ta. Another difference between the two films is the presence of (310) and (321) parasitic out-of-plane orientations in the HT film besides (110), whereas (110) is the only orientation detected in the RT film. We also note the presence of rings in the pole figures in Fig. 2b, c that demonstrate the lack of long-range in-plane ordering in either film.

The distinct surface morphology of the films is observed using atomic-force microscopy (AFM) Fig. 3a, b. The surface of HT Ta is characterized by micron-size pyramidal structures with a highest peak-to-valley height (S_z) of 11 nm, whereas the RT Ta surface shows worm-like features with an S_z of 24 nm. Despite similar root-mean-square roughness, 1.28 nm for HT Ta and 1.32 nm for RT Ta, a larger relative increase of surface area is found for RT Ta (3% for RT and <0.01% for HT) due to the larger S_z and smaller feature size, which, in turn, results in a larger effective dielectric region at the surface of the RT Ta film that can contribute to the surface loss tangent.

Complementary information regarding the microstructure and morphology of the films can be obtained using electron backscattering diffraction (EBSD) and transmission Kikuchi diffraction (TKD) techniques. EBSD data for HT Ta, shown in Fig. 3c, d, reveal a variable orientation grain-to-grain but also within grains, and a median grain size of 15 µm that is estimated from the false-color, larger-scale grain map shown in (d). TKD was used for the smaller-grain RT film due to its higher spatial resolution than EBSD. A map of the growth direction is shown in (e) from a cross-section view of a lamella using the same color code as in (c). The grains are confirmed to grow in column along the [hh0] direction as represented in green, and the lateral grain size is found to be about three orders of magnitude smaller than HT Ta, approximately 15 nm.

The structure and morphology of the films also translate into the transport properties presented in Table 2. While T_c remains similar, the residual resistance ratio (RRR) of RT Ta is found to be an order of magnitude

Table 2 | Summary of transport properties

	T_c (K)	R_{300K} (Ω/□)	$R_{4.5K}$ (Ω/□)	RRR	L_k (fH/□)
HT Ta	4.30	1.57	0.078	20.4	25
RT Ta	4.45	2.94	1.16	2.6	360

Critical temperature (T_c), sheet resistance at 300 K and 4.5 K (R_{300K}, $R_{4.5K}$), residual resistance ratio (*RRR*) and sheet kinetic inductance (L_k) for HT and RT Ta films.

smaller than HT Ta as expected from the higher density of grain boundaries in the RT Ta film. The sheet kinetic inductance (L_k), which inversely depends on the superfluid density, is calculated from the sheet resistance measured above the critical temperature at 4.5 K ($R_{4.5K}$) on the resonator transmission line (>3000 squares) with $L_k = \hbar R_{5K}/1.76\pi k_b T_c$[28]. The difference in L_k by more than an order of magnitude between the two films match the shift in resonance frequency discussed in the previous section and suggests a lower superfluid density in RT Ta, in agreement with the idea of a higher density of defects and shorter mean free path in this film[29]. A larger L_k also means a greater kinetic inductance fraction and therefore a pronounced sensitivity of the resonator frequency to material non-uniformity such as resistivity or thickness. Other transport properties such as the carrier density and mean free path in the normal state, penetration depth, critical field and superconducting coherence length are given in Supplementary Table S2 for future reference.

Materials characterization: surface and interface chemistry

We now turn to the analysis of the native oxide layers and the metal-substrate interfaces. We start with a baseline characterization of the oxide species present at the surface of HT and RT Ta films treated with BOE using variable kinetic energy X-ray photoelectron spectroscopy (VKE-XPS). The relative concentration of the different oxidation states of Ta as a function of depth, shown in Fig. 4a, b, is derived from the deconvolution of a set of Ta 4*f* XPS data measured for 14 values of the incident photon energy between 400 eV and 6000 eV. See the Supplementary Material for a detailed description of the data analysis. For both films, the native oxide is found to have an outermost Ta_2O_5 layer and a transition layer of suboxides at the interface with Ta, in agreement with recent studies of the surface chemistry of Ta[11,30]. The RT Ta film shows a thicker native oxide overall and a thicker suboxide layer in particular, which is confirmed by the values of the effective oxide thickness (h_{ox}) calculated from a multi-layer model, also shown in Fig. 4a, b.

Insights into the spatial distribution of the native oxide regions in fabricated devices are provided by the oxygen EELS maps in Fig. 4c, d and the corresponding line scans shown in the Supplementary Fig. S9. The measurements were carried out on cross-sections of resonator traces made from HT Ta and RT Ta films. Fabrication appears to have caused the native oxide to grow thicker for both films, albeit in substantially different ways. While both Ta traces present a 5-nm-thick O-rich outermost layer, the interface between this layer and Ta underneath is sharp for HT Ta but presents Ta-O intermixing in RT Ta, primarily along the grain boundaries. We note that suboxides had also been shown to form along the grain boundaries of Nb films[31]. Additional STEM images of the sidewalls are provided in Supplementary Fig. S10. Turning to the metal-substrate interface, a 5-nm-thick amorphous interdiffusion layer between Ta and Si is observed in the HT Ta resonator, in contrast with a sharper Nb/Si interface, albeit potentially not completely free of diffusion, in the RT Ta resonator. This disordered Ta-Si interdiffusion layer in HT Ta is a likely host for structural defects[32,33]. The STEM images provided in Fig. 4c, d also reveal the resonator sidewall angles and overetch depth in the silicon substrate, which are approximately 55° and 87 nm for HT Ta, and 80° and 62 nm for RT Ta. These differences reflect the impact of the interplay between the film morphology and the etch process, and lead to different interface participation ratios as shown in the simulations presented in Supplementary Fig. S2.

Discussion

Two clear differences between the properties of the RT Ta and HT Ta films emerge from our multimodal characterization study. On the one hand, the higher density of grain boundaries in the RT Ta films, caused by an average grain size smaller by three orders of magnitude than HT Ta, creates pathways for oxygen diffusion. In devices fabricated from RT Ta films, this results in oxygen contamination and the formation of amorphous Ta suboxides extending several tens of nm below the surface along the grain boundaries. On the other hand, the RT Ta films benefit from a sharper metal-substrate interface than the HT films, which show a Ta-Si interlayer. Both oxygen diffusion in RT Ta and Ta-Si interdiffusion in HT Ta result in an increase in the density of local chemical and structural defects that are commonly associated with dielectric loss.

Although we cannot exclude the possibility that the above-mentioned phenomena would yield comparable TLS loss in the two types of films, the more likely scenario is that loss is not dominated by the metal-air top surface and metal-substrate interface. Another potential candidate is the metal-air interface along the sidewalls, which likely hosts additional microscopic structural and chemical defects induced by the dry-etch process[34,35]. If the loss tangent was dominated by the contribution from these defects, the resonator quality factor would become insensitive to the thickness of the metal oxide layer. This would be consistent with the recent observation that suppressing the top native oxide layer of Ta resonators using gold capping does not result in an improvement of the quality factor[36]. A second candidate is the substrate–air interface. In addition to dry-etch induced damages, we also expect several angstroms of silicon oxide to have regrown in the day between the end-of-line buffered oxide etch and device loading in the dilution refrigerator[37]. Given the higher reported values for the loss tangent of silicon oxide[37] than tantalum oxide[22], it is plausible that the silicon oxide layer dominates dielectric loss for both devices, regardless of the sputtering method used for Ta. We finally consider the role of the silicon substrate. The measured TLS-induced loss does not increase proportionally with interface participation ratios between $w = 30$ μm and $w = 3$ μm, suggesting an influence from TLSs residing within the silicon substrate rather than exclusively at interfaces.

While we cannot provide a definite explanation for the comparable performance of the two types of films based on our current data, the fact that there is no clear correlation between a number of material properties and resonator performance helps narrow down the range of candidate mechanisms for dominant sources of loss in state-of-the-art Ta superconducting resonators. It is corroborated by other recent studies that have demonstrated similar resonator performance for different grain sizes of Ta on sapphire[38], and quality factors in the 10^6 range for polycrystalline Ta grown on silicon at cryogenic temperatures[39]. Our results not only highlight the robustness of the low loss of α-Ta with regard to the film structural and transport properties, but they also suggest that the thickness and disorder of the surface metal oxides do not correlate with device performance[31,40] for Ta-based devices in the low 10^{-7} single-photon-level loss regime.

Conclusion

We have shown that resonators fabricated from α-tantalum films grown on silicon at room temperature on a Nb seed layer can perform as well as the current state-of-the-art resonators fabricated from films grown at high temperature. Irrespective of the growth process temperature, our resonators yield state-of-the-art losses in the single photon regime, with median values in the low 10^{-7}. Profound differences are found in the material properties of these two types of films, including a three-orders-of-magnitude difference in their grain size, significant oxygen diffusion from the metal–air interface in the room-temperature film, a one-order-of-magnitude difference in RRR and kinetic inductance, and interdiffusion at the metal–substrate interface in the high-temperature film. To interpret our findings, we suggest that TLS loss in our Ta-based superconducting resonators is dominated by other mechanisms than these properties, such as the fabrication-induced defects along the sidewalls, the surface oxides and fabrication-induced defects at the substrate–air interface, and defects in the silicon substrate. In addition to

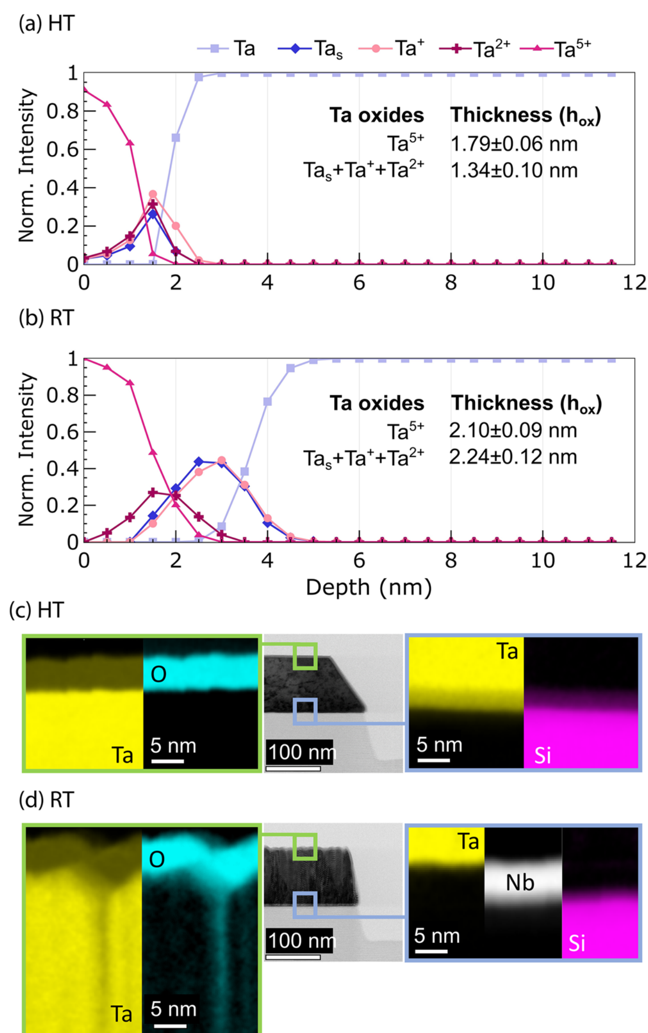

Fig. 4 | Surface and interface composition. Depth profile of the tantalum oxide composition at the surface of HT Ta (**a**) and RT Ta (**b**) films, extracted from energy-dependent x-ray photoelectron spectroscopy. Estimates of the oxide layer thicknesses (h_{ox}) and their error bars, associated to different Ta valence states and derived from a multi-layer model, are also shown in (**a**) and (**b**). **c**, **d** Bright-field transmission electron microscopy view (TEM) and electron energy-loss spectroscopy (EELS) composition analysis of the cross-section of a resonator made from HT Ta (**c**) and RT Ta (**d**).

highlighting potential areas of further improvements for Ta-based superconducting circuits, our study shows that α-Ta sputtered at room temperature is a potent material for integration into high-performance superconducting qubits. Its use should be particularly beneficial for applications that require either a high process throughput or compatibility with low-thermal budget fabrication processes, and which can accommodate the larger kinetic inductance.

Methods

Fabrication

The films were deposited using a magnetron DC sputtering system from Angstrom Engineering on 4-in. high-resistivity silicon wafers (>20 kΩ cm). Prior to deposition, the wafers were treated in a buffered oxide etchant (BOE 10:1) solution to remove the native oxide layer. The base pressure of the deposition chamber was under 2×10^{-7} Pa, and the purity of the tantalum and niobium targets was respectively 99.998% and 99.99%. The substrate was either heated at 350 °C (as measured at the substrate surface) or kept at room temperature during deposition of the HT and RT films, respectively. The total thickness of the films is 100 nm, which includes a 5-nm-thick Nb buffer layer for the RT films, and the deposition rate is on the order of 8 nm/min.

The metal-coated wafers were then cleaned with an oxygen plasma for 10 min at 150 W, dehydrated on a hotplate at 140 °C, and coated with vapor hexamethyldisilazane before being baked again at 140 °C. The SPR955 resist was spun and baked at 100 °C, patterned with a direct write optical lithography method (MLA150 Heidelberg) and developed with an MF319 solution. The films were finally etched with a two-step sequence including Ar milling and inductively coupled plasma reactive ion etching with chlorine-based chemistry, and cleaned with an oxygen plasma followed by an EKC chemical treatment. After dicing the wafers, the chips selected for cryogenic RF measurements were again cleaned with acetone, IPA, oxygen plasma, and a last BOE 10:1 treatment prior to packaging.

Film characterization

The structural properties of the films were first characterized with XRD using Cu Kα radiation in a parallel-beam configuration on a Rigaku Smartlab diffractometer. The morphologies and elemental distributions at the interfaces of resonator devices were imaged using scanning transmission electron microscopy and electron energy loss spectroscopy with an FEI probe-corrected TITAN operated at 200 kV, on 70-nm thick lamellae prepared with the plasma-focused ion beam lift-out technique. Depth profiles of the Ta oxide species near the film surfaces were obtained using VKE-XPS. The VKE-XPS measurements were performed at the NIST Spectroscopy Soft and Tender (SST-1 and SST-2) beamlines at the National Synchrotron Light Source II in Brookhaven National Laboratory. The grains in the films were characterized with a Dimension Icon atomic force microscope (AFM) from Bruker in a PeakForce scanning mode, and through EBSD and TKD in a Thermo Fisher Helios 5 UC scanning electron microscope equipped with an e-flash FS detector and EBSD or Optimus 2 TKD detector head. The transport measurements were performed in a Quantum Design DynaCool physical property measurement system, from room temperature to 1.8 K, and with a magnetic field oriented along the normal of the samples.

Device design and measurements

The 10 mm × 10 mm resonator chips consist of 12 side-coupled $\lambda/4$ CPW resonators connected to one transmission line. The measurements were carried out using a vector network analyzer in a conventional setup[41], which consists of 75 dB total input attenuation on the input line and a cryogenic low noise amplifier followed by a room-temperature amplifier on the output line. The internal quality factors (Q_i) or loss (δ_i) were extracted from the measurements of the transmission signal S_{21} of transmission lines inductively coupled to resonators and analyzed with a diameter correction method (DCM) method described in ref. 42. All the resonators are measured at least 70 times, and the losses reported in the manuscript, between 15 and 70 points per resonator, are down-selected from this initial pool of data based on the fit quality and photon number, which is constrained to the 1 ± 0.5 photon number for the single-photon regime.

Data availability

The authors declare that the data supporting the findings of this study are available within the paper and its supplementary information files.

Received: 30 January 2025; Accepted: 22 July 2025;
Published online: 16 August 2025

References

1. Krinner, S. et al. Realizing repeated quantum error correction in a distance-three surface code. *Nature* **605**, 669–674 (2022).
2. Acharya, R. et al. Suppressing quantum errors by scaling a surface code logical qubit. *Nature* **614**, 676–681 (2023).
3. Sundaresan, N. et al. Demonstrating multi-round subsystem quantum error correction using matching and maximum likelihood decoders. *Nat. Commun.* **14**, 2852 (2023).

4. Acharya, R. et al. Quantum error correction below the surface code threshold. *Nature* **638**, 920–926 (2025).
5. Shor, P. W. Scheme for reducing decoherence in quantum computer memory. *Phys. Rev. A* **52**, R2493–R2496 (1995).
6. Knill, E., Laflamme, R. & Zurek, W. H. Resilient quantum computation. *Science* **279**, 342–345 (1998).
7. Milne, J. G. C. Superconducting transition temperature of high-purity tantalum metal. *Phys. Rev.* **122**, 387–388 (1961).
8. Place, A. P. M. et al. New material platform for superconducting transmon qubits with coherence times exceeding 0.3 milliseconds. *Nat. Commun.* **12**, 1779 (2021).
9. Wang, C. et al. Towards practical quantum computers: transmon qubit with a lifetime approaching 0.5 milliseconds. *npj Quantum Inf.* **8**, 1–6 (2022).
10. Ganjam, S. et al. Surpassing millisecond coherence in on chip superconducting quantum memories by optimizing materials and circuit design. *Nat. Commun.* **15**, 3687 (2024).
11. McLellan, R. A. et al. Chemical profiles of the oxides on tantalum in state-of-the-art superconducting circuits. *Adv. Sci.* **10**, 2300921 (2023).
12. Face, D. W., Ruggiero, S. T. & Prober, D. E. Ion-beam deposition of Nb and Ta refractory superconducting films. *J. Vac. Sci. Technol. A Vac. Surf. Films* **1**, 326–330 (1983).
13. Face, D. W. & Prober, D. E. Nucleation of body-centered-cubic tantalum films with a thin niobium underlayer. *J. Vac. Sci. Technol. A Vac. Surf. Films* **5**, 3408–3411 (1987).
14. Alegria, L. D. et al. Two-level systems in nucleated and non-nucleated epitaxial alpha-tantalum films. *Appl. Phys. Lett.* **123**, 062601 (2023).
15. Singer, M. et al. Tantalum thin films sputtered on silicon and on different seed layers: material characterization and coplanar waveguide resonator performance. In: *Proc. 5th IEEE International Conference on Quantum Computing and Engineering, QCE 2024*—Montreal, Canada. 15–20 September 2024 (Institute of Electrical and Electronics Engineers Inc., 2024).
16. Barends, R. et al. Niobium and tantalum high Q resonators for photon detectors. *IEEE Trans. Appl. Supercond.* **17**, 263–266 (2007).
17. Urade, Y. et al. Microwave characterization of tantalum superconducting resonators on silicon substrate with niobium buffer layer. *APL Mater.* **12**, 021132 (2024).
18. Poorgholam-Khanjari, S. et al. Engineering high-Q superconducting tantalum microwave coplanar waveguide resonators for compact coherent quantum circuits. *Sci. Rep.* **15**, 27113 (2024).
19. Lozano, D. P. et al. Low-loss α-tantalum coplanar waveguide resonators on silicon wafers: fabrication, characterization and surface modification. *Mater. Quantum Technol.* **4**, 025801 (2024).
20. Shi, L. et al. Tantalum microwave resonators with ultra-high intrinsic quality factors. *Appl. Phys. Lett.* **121**, 242601 (2022).
21. Grigoras, K. et al. Qubit-compatible substrates with superconducting through-silicon vias. *IEEE Trans. Quantum Eng.* **3**, 1–10 (2022).
22. Crowley, K. D. et al. Disentangling losses in tantalum superconducting circuits. *Phys. Rev. X* **13**, 041005 (2023).
23. Phillips, W. A. Two-level states in glasses. *Rep. Prog. Phys.* **50**, 1657–1708 (1987).
24. Anderson, P. W., Halperin, B. I. & Varma, cM. Anomalous low-temperature thermal properties of glasses and spin glasses. *Philos. Mag.* **25**, 1–9 (1972).
25. Burnett, J., Faoro, L. & Lindström, T. Analysis of high-quality superconducting resonators: consequences for TLS properties in amorphous oxides. *Supercond. Sci. Technol.* **29**, 044008 (2016).
26. Gao, R. et al. Epitaxial titanium nitride microwave resonators: structural, chemical, electrical, and microwave properties. *Phys. Rev. Mater.* **6**, 036202 (2022).
27. Murray, C. E. Material matters in superconducting qubits. *Mater. Sci. Eng. R Rep.* **146**, 100646 (2021).
28. Annunziata, A. J. et al. Tunable superconducting nanoinductors. *Nanotechnology* **21**, 445202 (2010).
29. Glezer Moshe, A., Farber, E. & Deutscher, G. Granular superconductors for high kinetic inductance and low loss quantum devices. *Appl. Phys. Lett.* **117** https://pubs.aip.org/apl/article/117/6/062601/39425/Granular-superconductors-for-high-kinetic (AIP Publishing, 2020).
30. Mun, J. et al. Probing oxidation-driven amorphized surfaces in a Ta(110) film for superconducting qubit. *ACS Nano* **18**, 1126–1136 (2024).
31. Premkumar, A. et al. Microscopic relaxation channels in materials for superconducting qubits. *Commun. Mater.* **2**, 1–9 (2021).
32. Nakayama, T. & Kobinata, K. Physics of Schottky-barrier change by segregation and structural disorder at metal/Si interfaces: first-principles study. *Thin Solid Films* **520**, 3374–3378 (2012).
33. Cheng, J. Y., Wang, M. H. & Chen, L. J. Formation of amorphous interlayers by solid-state diffusion in refractory metal/silicon systems. *MRS Online Proc. Libr.* **187**, 77–82 (1990).
34. Uejima, K. & Umeda, T. Microscopic origins of dry-etching damages in silicon large-scaled integrated circuits revealed by electrically detected magnetic resonance. *Appl. Phys. Lett.* **104**, 082111 (2014).
35. Cao, Y. et al. Surface quality and microstructure evolution in fused silica under SF6/Ar reactive ion beam etching. *J. Non-Crystal Solids* **641**, 123144 (2024).
36. Chang, R. D. et al. Eliminating surface oxides of superconducting circuits with noble metal encapsulation. *Phys. Rev. Lett.* **134**, 097001 (2024).
37. Morita, M., Ohmi, T., Hasegawa, E., Kawakami, M. & Ohwada, M. Growth of native oxide on a silicon surface. *J. Appl. Phys.* **68**, 1272–1281 (1990).
38. Jones, S. G. et al. Grain size in low-loss superconducting Ta thin films on c-axis sapphire. *J. Appl. Phys.* **134**, 144402 (2023).
39. van Schijndel, T. A. J. et al. Cryogenic growth of tantalum thin films for low-loss superconducting circuits. *Phys. Rev. Appl.* **23**, 034025 (2024).
40. Altoé, M. V. P. et al. Localization and mitigation of loss in niobium superconducting circuits. *PRX Quantum* **3**, 020312 (2022).
41. McRae, C. R. H. et al. Materials loss measurements using superconducting microwave resonators. *Rev. Sci. Instrum.* **91**, 091101 (2020).
42. Khalil, M. S., Stoutimore, M. J. A., Wellstood, F. C. & Osborn, K. D. An analysis method for asymmetric resonator transmission applied to superconducting devices. *J. Appl. Phys.* **111**, 054510 (2012).

Acknowledgements

This research used the NIST-operated Spectroscopy Soft and Tender Beamlines (SST-1 and SST-2) of the National Synchrotron Light Source II, U.S. Department of Energy (DOE) Office of Science User Facilities operated for the DOE Office of Science by Brookhaven National Laboratory under Contract No. DE-SC0012704. Certain commercial equipment, instruments, or materials are identified in this paper in order to specify the experimental procedure adequately, and do not represent an endorsement by the National Institute of Standards and Technology. We thank Simone Severini, Bill Vass, James Hamilton, Peter DeSantis, Fernando Brandao, Eric Chisholm, Matthew Matheny, and Shmulik Eisenmann at AWS for their involvement and support of the research activities at the AWS Center for Quantum Computing.

Author contributions

The study was designed and led by G.M. and I.J. The tantalum films were developed by G.M. and I.J. The structural properties, grain morphology, and surface roughness of the films were characterized by G.M., S.D., N.M., and V.L. The transport properties of the films were measured by G.M. The energy-dependent XPS data were collected by C.W., with support from C.J., A.K.R., and D.A.F., and analyzed by E.U., C.W., and I.J. The TEM-EELS data

were interpreted by G.M., I.J., and M.H. The design of the resonators was developed by S.A. and R.R., and their fabrication was led by N.D. and Y.H. The resonator measurements were performed by C.C., D.P., J.G., and the interpretation of the data was led by G.M., with support from C.C., O.P., J.G., D.P., and I.J. The interpretation of all the data presented in the paper was led by G.M. and I.J., with support from O.P. The manuscript was written by G.M. and I.J. and reviewed by all co-authors.

Competing interests

The authors declare no competing interests.

Additional information

Supplementary information The online version contains supplementary material available at https://doi.org/10.1038/s43246-025-00897-x.

Correspondence and requests for materials should be addressed to Guillaume Marcaud or Ignace Jarrige.

Peer review information *Communications Materials* thanks Marco Arzeo and the other, anonymous, reviewer(s) for their contribution to the peer review of this work. Primary Handling Editors: Nicola Poccia and Aldo Isidori. A peer review file is available.

Reprints and permissions information is available at http://www.nature.com/reprints

Publisher's note Springer Nature remains neutral with regard to jurisdictional claims in published maps and institutional affiliations.

Open Access This article is licensed under a Creative Commons Attribution 4.0 International License, which permits use, sharing, adaptation, distribution and reproduction in any medium or format, as long as you give appropriate credit to the original author(s) and the source, provide a link to the Creative Commons licence, and indicate if changes were made. The images or other third party material in this article are included in the article's Creative Commons licence, unless indicated otherwise in a credit line to the material. If material is not included in the article's Creative Commons licence and your intended use is not permitted by statutory regulation or exceeds the permitted use, you will need to obtain permission directly from the copyright holder. To view a copy of this licence, visit http://creativecommons.org/licenses/by/4.0/.

© The Author(s) 2025, modified publication 2026